Materials & Design 231 (2023) 112043

Contents lists available at ScienceDirect

Materials & Design

journal homepage: www.elsevier.com/locate/matdes

The role of graphene in Graphene-Filled carbon nanotube foam under compression and the corresponding microscopic deformation mechanism

Shuai Wang [a], Chao Wang [b,d], Lihong Liang [a,*], Shaohua Chen [c,*]

[a] College of Mechanical and Electrical Engineering, Beijing University of Chemical Technology, Beijing 100029, China
[b] LNM, Institute of Mechanics, Chinese Academy of Sciences, Beijing 100190, China
[c] Institute of Advanced Structure Technology, Beijing Institute of Technology, Beijing 100081, China
[d] School of Engineering Science, University of Chinese Academy of Sciences, Beijing 100049, China

HIGHLIGHTS

- The role of graphene in the graphene-filled carbon nanotube foam under compression is elucidated.
- The carbon nanotubes in the foam become more dispersed due to the adhesion and separation effect of graphene.
- The graphene flakes act as fixed support to improve the bending ability of carbon nanotubes.
- The modulus improves significantly with the number of graphene flakes but is hardly sensitive to the thickness of graphene.

GRAPHICAL ABSTRACT

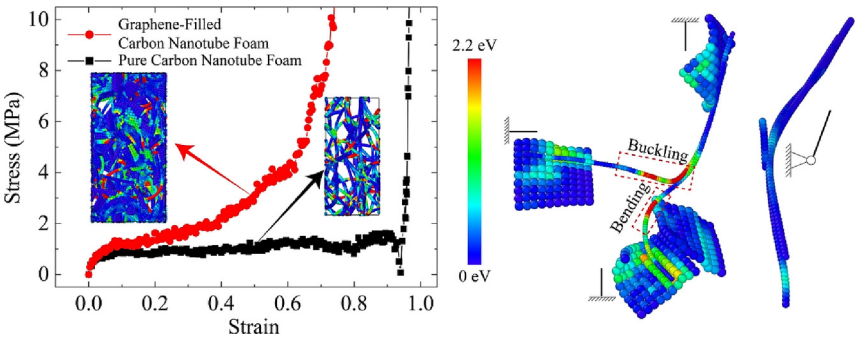

ARTICLE INFO

Article history:
Received 28 November 2022
Revised 12 May 2023
Accepted 25 May 2023
Available online 30 May 2023

Keywords:
Carbon nanotube foam materials
Graphene
Compression
Microscopic deformation mechanism

ABSTRACT

Graphene-filling significantly improves the compressive properties of carbon nanotube (CNT) foam (CF). However, the role of graphene in the graphene-filled CNT foam (GFCF) and the corresponding microscopic deformation mechanism, are still unclear. Here, coarse-grained numerical models of pure CF and GFCF are constructed based on molecular dynamics, and the role of graphene in GFCF and corresponding microscopic deformation mechanisms under compression are investigated. It is found that the compressive modulus of GFCF (5.3 MPa) is much larger than that of pure CF (0.7 MPa). The filling of graphene inhibits the aggregation of CNTs, enhances the dispersion of CNTs, impedes the rearrangement of CNTs, and ultimately improves the compressive modulus of the whole material by improving the bending ability of CNTs. It is further found that the compressive modulus of GFCF can be increased to a maximum of 7.4 MPa as the number of graphene flakes increases to 300, but remains almost the same as the graphene thickness increases. The results in this paper deepen the understanding of the microscopic mechanisms of GFCF and provide scientific guidance for the application of CNT and graphene-based materials.

1. Introduction

As the most typical one-dimensional (1D) and two-dimensional (2D) nanomaterials, carbon nanotubes [1] (CNT) and graphenes [2]

* Corresponding authors.
E-mail addresses: lianglh@mail.buct.edu.cn (L. Liang), shchen@bit.edu.cn (S. Chen).

https://doi.org/10.1016/j.matdes.2023.112043
0264-1275/

have attracted extensive attention due to their unique mechanical, electrical, and thermal properties, enable it a wide range of application prospects [3], and the corresponding preparation method is also getting a lot of attention [4]. To extend their excellent properties to the macroscopic world, three-dimensional (3D) foam materials composed of CNT or graphene are constructed, both of which exhibit low density [5,6], large surface area [7], high porosity [8], excellent electrical conductivity [9], high thermal conductivity [10], etc., enabling wide potential applications in energy conversion and storage devices [11], flexible electronics [12], supercapacitors [13], sensors [14], and so on. The applicability of pure CNT foam (CF) or graphene foam (GrF) remains questionable due to its poor mechanical characteristics [15], which will be significantly improved by combining CNTs and graphene to form graphene/CNT composite foam. For instance, the graphene/CNT composite foams possess ultralow densities as low as 0.16 mg/cm^3 [16], enable superb stretchability up to 200% elongation [17], and support 3150 times the foam's weight with reversible height change [18], further extending their application prospects. Therefore, the underlying mechanism by which graphene/CNT composite foams possess outstanding properties and the strategies to improve their mechanical properties have attracted extensive attention.

One strategy to improve the mechanical properties of graphene/CNT composite foams is to enhance the intrinsic properties of their internal components. For example, Vinod et al. [19] pointed out that the mechanical failure of foam materials is related to the vertical graphene cell walls, and therefore can be strengthened by replacing the soft graphene with stiffer CNTs. In addition, some researchers introduced CNTs onto the graphene surface to form CNT-coated graphene flakes, Sun et al. [16] point out that the CNT-coated graphene flakes have a higher recovery capacity compared to flexible graphene cell walls, so the resulting composite foam material has higher compressive elasticity; Wang et al. [20] numerically confirmed that the bending stiffness of CNT-coated graphene flakes is also higher, leading to a larger compressive modulus. Furthermore, Yan et al. [21] and Hacopian et al. [22] developed CNT-coated graphene with covalently bonded CNTs and graphene, where CNTs act as reinforcing bars toughening graphene and hence term it "rebar graphene". Based on this, Sha et al. [18] further synthesized 3D rebar GrF with higher structural stability, strength, and storage modulus.

Another strategy is to connect CNTs and graphene into continuous structures to fully exploit the intrinsic properties of CNTs and graphene. Typical examples are the graphene/CNT composite foams with vertically aligned structures [23,24], in which CNTs are vertically attached to graphene sheets through covalent bonds, resulting in super-elasticity [25], outstanding electronic transport properties [26], and excellent hydrogen storage capacity [27] due to their theoretically perfect structure. In addition, Guo et al. [17] obtained a highly stretchable graphene/CNT composite foam with a retractable 200% elongation by bonding CNTs with graphene sheets to prevent crack propagation and brittle breakage. Kuang et al. [28] fabricated the composite foam with higher specific strength, elasticity and mechanical stability, and they attribute the excellent performance to the continuous structure formed as long and entangled CNTs weave graphene together. Kim et al. [29] fabricated graphene-coated CNT foams, in which graphene accumulated at the nodes between the CNTs, strengthening the nodes and thus generating an approximately sixfold increase in both Young's modulus and the storage modulus. Wang et al. [30] investigated the microscopic deformation mechanism of CNT-bonded graphene foam interconnected by long CNT and short crosslinkers.

Besides, CNTs and graphene could largely prevent the aggregation of each other, resulting in the improvement of their structural stability and mechanical robustness [31,32]. For example, Yang et al. [33] stated that the long and tortuous CNTs can bridge adjacent graphene and inhibit their aggregation, resulting in a high contact area in the foams; Kabiri et al. [34] incorporated CNTs into GrFs to effectively avoid the aggregation of graphene sheets and increase the robustness of the resulting composite; Bagotia et al. [35] proposed that CNTs bridge the gaps between the graphene and inhibit the face to face aggregation of graphene, leading to a synergetic improvement in composite properties; Ye et al. [36] prepared the graphene-winged CNTs by a well-controlled outer-wall peeling process of multiwalled CNTs, in which the outer graphene could suppress the aggregation of CNTs, and the CNT could bridge the graphene to enhance the mechanical robustness.

The existing mechanisms mainly focus on the intrinsic properties of the internal components [20] and the connections between them [28], although many researchers realized that the aggregation of CNT and graphene seriously limits their practical applications [37], the role of graphene in the structural dispersity and mechanical properties of the composite foam, and corresponding microscopic deformation mechanism under compression, are still unclear. In this paper, we established a mesoscopic numerical model of pure CF and graphene-filled CNT foam (GFCF) and revealed the underlying mechanism by investigating the effect of graphene-filling on the aggregation and deformation of CNTs.

2. Coarse-grained models of pure CF and GFCF

To simulate the mesoscale physical processes and cost-effectively retain the microscale details, coarse-grained models are adopted, where atoms are clustered into beads that interact through effective force fields. The coarse-grained graphene [38,39] and CNT [40,41] models are combined to describe the deformation of their respective deformation and the interaction among them. The validity of coarse-grained models of graphene foam [42–44], CNT network [45,46], and their combined systems [20,30] have been verified in previous works.

To describe the bending and stretching deformation of CNTs, two harmonic potential functions, i.e., $E_{cb} = k_{cb}\,(\theta_c - \theta_{c0})^2/2$ and $E_{ct} = k_{ct}\,(r_c - r_{c0})^2/2$, are adopted, in which the variable parameters θ_c and r_c are the current bending angle and the current bond length in CNT; the constant parameters k_{cb}, θ_{c0}, k_{ct}, r_{c0}, are the bending stiffness, the equilibrium bending angle, the stretching stiffness, and the equilibrium bond length in CNT, respectively. To characterize the stretching, bending and shearing deformation of graphene, three harmonic potential functions $E_{gt} = k_{gt}\,(r_g - r_{g0})^2/2$, $E_{gb} = k_{gb}\,(\theta_g - \theta_{g0})^2/2$, and $E_{gs} = k_{gs}\,(\varphi_g - \varphi_{g0})^2/2$ are adopted, where the variable parameters r_g, θ_g, and φ_g are the current bond length, the current bending angle and the current shearing angle in graphene, respectively. The constant parameters k_{gt}, r_{g0}, k_{gb}, θ_{g0}, k_{gs}, and φ_{g0} are the tensile stiffness, the equilibrium bond length, the bending stiffness, the equilibrium bending angle, the shearing stiffness, and the equilibrium shearing angle in graphene, respectively.

In experiments, Van der Waals forces, hydrogen bonding [47], functional groups [48,49], ions [50], and even covalent bonding [22] may exist, which are usually described by bonded and non-bonded interactions in coarse-grained molecular dynamics simulation. The bonded and non-bonded interactions are usually simulated by crosslinkers and Van der Walls interaction, respectively. The crosslinkers have a significant effect on the tensile properties of CNT/graphene composite foams [30], but have less effect in our compression model as discussed in Fig. S1 of Supplemental Materials. Therefore, the Van der Waals interaction is mainly considered, which is depicted by a Lennard-Jones (LJ) potential function $E_{vdW} = 4\varepsilon\,((\sigma/r)^{12} - (\sigma/r)^6)$. The parameters σ and ε and are the zero-energy distance and the energy well depth, which varies depending on the type of beads, and the effect of interaction

strength of graphene flakes and CNTs are discussed in Fig. S1 of Supplemental Materials. The main force-field parameters of single-walled CNT and single-layer graphene are listed in Table 1.

The CNT and graphene-based foam can be prepared by a variety of synthesis methods [28,51,52], resulting in various microstructures. The formatting process can be simulated to investigate the topological structures [53], and the relationship between the microstructures and corresponding mechanical properties can be clarified by developing numerical models with various initial structures, such as entangled CNT foam [54], the CNT foam containing binders [45], randomly oriented graphene foam [43], honeycomb-like graphene foam [55], CNT-coated graphene foam [20], and CNT-bonded graphene foam [30]. In this paper, a typical numerical model of the GFCF is constructed to further explore the role of graphene when it is introduced into CNT foam.

As shown in Fig. 1a, the GFCF consists of 100 CNT chains with an average length of ~100 nm and 100 square graphene flakes with an average side length of ~ 25 nm. A coarse-grained CNT chain contains 100 CNT beads as shown in Fig. 1b-I; to show its local structure clearly, an enlarged configuration of the CNT chain is illustrated in Fig. 1b-II, where every CNT bead denotes a single-walled CNT with a length of 1 nm shown in Fig. 1b-III. Correspondingly, every graphene flake in the coarse-grained model contains 100 graphene beads as illustrated in Fig. 1b-IV, where every graphene bead denotes single-layer graphene with a side length of 2.5 nm shown in Fig. 1b-V. Note that the size of graphene and CNT in our simulation is much smaller than that in real experiments, which makes it difficult to compare quantitatively with experiments. However, the microscopic structures observed in the experiment can be qualitatively simulated, and the microscopic deformation mechanism can be revealed. This method has been used in a series of studies by Wang et al.[25,53,56], Xie et al. [57], Xiao et al. [58,59], and our group [42–44].

To evaluate the effect of the number of graphene flakes, the initial models of GFCF containing 100, 50, and 10 graphene flakes are established, as shown in Fig. 1c-I, -II, and -III, respectively, where the number and the initial structure of the CNT chains are set to be the same, with graphene merely added into the pores. Since graphene is smaller than the CNT, the graphene filled in the pores tends to be unconnected, even for a GFCF with the same amount of CNT and graphene beads as shown in Fig. 1c-I, the graphene is still not completely connected. Instead, the CNTs are fully connected and wound together as a whole to act as the main skeleton in GFCF, whose structure is also the same as the initial model of pure CF shown in Fig. 1c-IV.

To achieve a steady state, the system is firstly relaxed at a constant temperature of 300 K and pressure of 1 atmosphere using the isothermal–isobaric ensemble (NPT) technique. During the relaxation, the periodic boundary conditions are applied in all three directions. The steady state after relaxation is shown in Fig. 1d, where the structure of CNT in GFCF containing 100 CNT chains and 100 graphene flakes (Fig. 1d-I) is still almost the same as its initial structure shown in Fig. 1c-I. However, as the number of graphene flakes decreases, the initially dispersed CNTs gradually tend to form CNT bundles as shown in Fig. 1c-II and -III, especially for the pure CF that is shown in Fig. 1c-IV, where most CNT exist as bundles. This means the dispersed CNTs are quite capable of forming bundles, but are possible to maintain the form of dispersed CNTs due to the filling of graphene. The phenomenon that the aggregation of CNT and graphene are inhibited is quite common in experiments[31–33,36], however, the corresponding mechanism and its effect on the mechanical property of the whole materials are still unclear, which are investigated in the following. The density of the relaxed simulation model is about 12 ~ 22 mg/cm^3, which is in accord with the density range of 0.16 ~ 64 mg/cm^3 measured in experiments [16,29,60].

After the relaxation, uniaxial compressive loading with a strain rate of ~10^7 s^{-1} is applied in the *x*-direction, the Langevin thermostat 300 K is still adopted during the compression, but the Berendsen barostat 1 Pa is only adopted in the *y* and *z*-directions. In all simulations, the time step and cutoff distance are set as 10 fs and 3 nm. All simulations are implemented by an open-source software Large-scale Atomic/Molecular Massively Parallel Simulator (LAMMPS) [61], and all the figures are illustrated by using the open-source software Ovito [62].

3. Results and discussion

3.1. Stress–strain relationship of pure CF and GFCF

The compressive stress–strain curve of GFCF composed of 100 graphene flakes and 100 CNT chains is shown in Fig. 2a, and the curve of a pure CF with the same number of CNT chains is also shown for comparison, both of which can be divided into three stages according to the slope of stress, i.e., initial, platform, and compaction stage, this trend is consistent with the stress–strain curves of graphene foams [43] and graphene/CNT composite foams [20,30]. The corresponding secant modulus as a function of strain is also calculated and shown in Fig. S2 of Supplemental Materials to investigate the change in stress, which shows that the modulus in the platform stage is smaller than that in the initial and compaction stages.

In the initial stage, i.e., when the strain is lower than 0.02, the stress of both pure CF and GFCF increases sharply. Amplification of the curves in this stage is shown in the inset of Fig. 2a, which shows that the stress of GFCF is slightly larger than that of pure CF. The moduli in this stage are named initial moduli and are measured as 21.1 and 25.8 MPa (Fig. S2), respectively, indicating that the introduction of graphene flakes slightly enhances the stiffness of GFCF compared to pure CF. As the strain increases to the platform stage, the stress of pure CF increases slowly, the average modulus obtained by linear fitting in the whole platform stage is about 0.7 MPa, much smaller than its initial modulus, and is named intermediate modulus. The intermediate modulus of GFCF is measured as 5.3 MPa, also smaller than its initial modulus but much larger

Table 1
The parameters of the main force field [38–41].

Parameters		Values	Parameters		Values
r_{c0} (Å)		10	k_{ct} (kcal mol^{-1} Å^{-2})		1000
θ_{c0} (rad)		180	k_{cb} (kcal mol^{-1} rad^{-2})		14,300
r_{g0} (Å)		25	k_{gt} (kcal mol^{-1} Å^{-2})		470
θ_{g0} (rad)		180	k_{gb} (kcal mol^{-1} rad^{-2})		144.9
φ_{g0} (rad)		90	k_{gs} (kcal mol^{-1} rad^{-2})		16,870
Parameters	Types of beads	Values	Parameters	Description	Values
ε	Gra-Gra	473.0	σ	Gra-Gra	23.84
(kcal/mol)	Gra-CNT	473.0	(Å)	Gra-CNT	23.84
	CNT-CNT	15.1		CNT-CNT	9.35

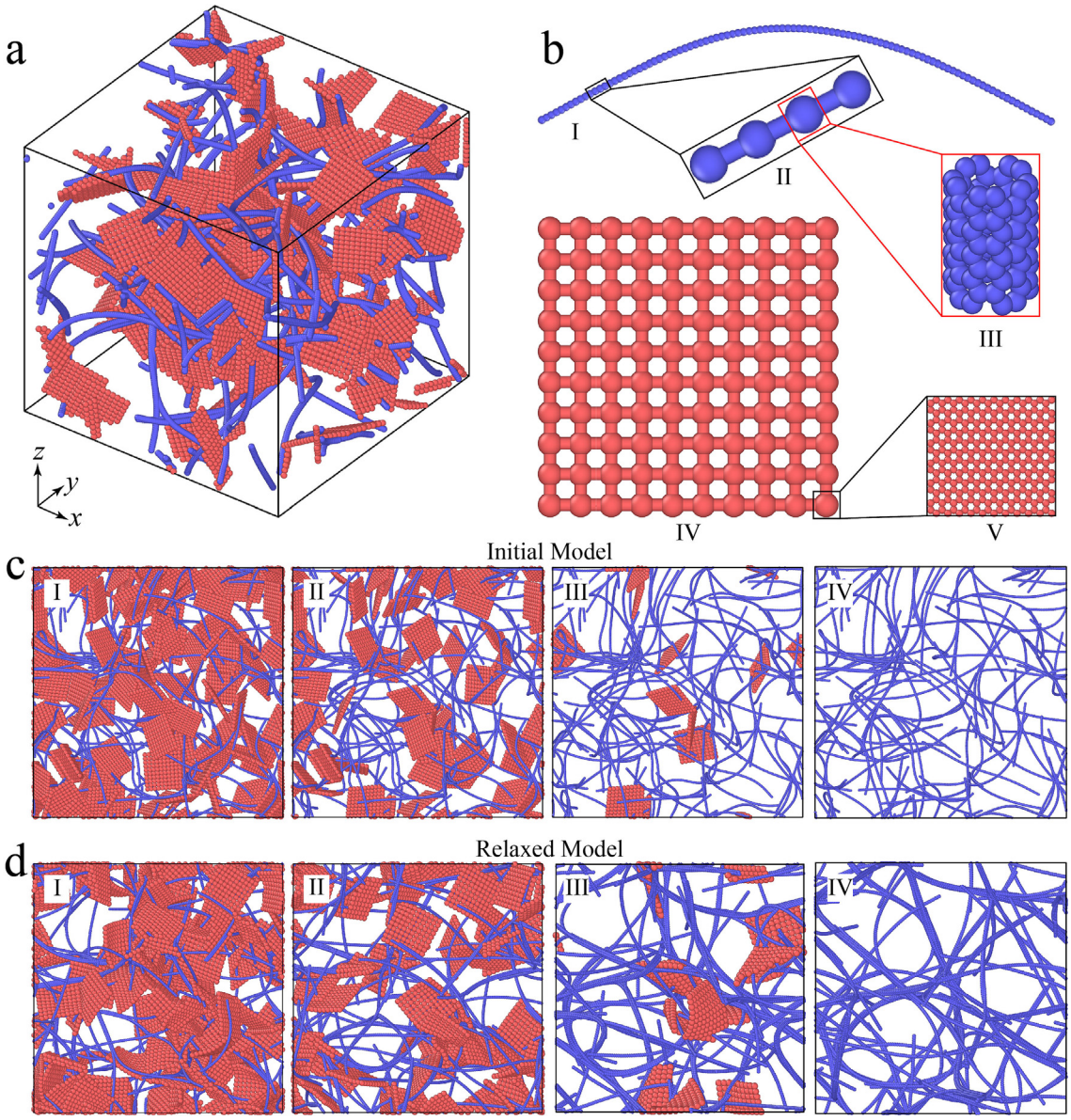

Fig. 1. The numerical models of GFCF and pure CF. (a) The 3D numerical model of GFCF consists of 100 graphene flakes and 100 CNT chains. (b) I: The coarse-grained model of a CNT chain; II: the partial enlarged drawing of the CNT chain; III: the full-atomic CNT with a length of 1 nm and chirality of (5, 5); IV: the coarse-grained model of a single-layer graphene flake; V: the full-atomic graphene with a side length of 2.5 nm. (c) The initial models of GFCF containing (I) 100, (II) 50, and (III) 10 graphene flakes and (IV) pure CF. (d) The relaxed models of GFCF containing (I) 100, (II) 50, and (III) 10 graphene flakes and (IV) pure CF.

than the intermediate modulus of pure CF. In other words, the introduction of graphene markedly enhances the stiffness of GFCF compared to pure CF in the platform stage. This is consistent with previous results [16,28] that the CNT/graphene composite foams have stronger compression performance than pure CF. As the strain increases further, more CNTs and graphene touch each other as the foam compresses, leading to more graphene and CNTs deforming, as well as an increase in the overall stress.

To completely show the stress–strain relationship in the compaction stage, the stress–strain curves of GFCF and pure CF with larger stress are shown in Fig. 2b, which shows that the stress increases significantly in this stage, and the moduli of both GFCF and pure CF exceed 100 MPa as shown in Fig. S2 of Supplemental Materials, much larger than the initial and intermediate modulus. However, the stress of GFCF increases with an increasing slope when the strain is between ~ 0.6 and ~ 0.8, after that, the stress increases significantly. As for pure CF, the transition from the platform stage to the compaction stage is more complicated: before compaction, there is a drop in stress when the strain is between ~ 0.9 and ~ 0.95.

The drop in stress of pure CF can be explained by the insets in Fig. 2b, which is colored by the local stress in the *x* direction. The snapshots color-coded by different color bar ranges are also shown in Fig. S3. Under a strain of 0.8, the part of the CNT along the *x* direction is buckling, supporting the compressive loading. However, the buckling part of the CNT gradually rotates, under a strain of 0.95, the CNT is almost perpendicular to the compression direction, and the CNT is no longer subjected to compressive stress, resulting in a sudden drop in stress.

It should be noted that the strain of pure CF (0.9 to 0.95) after which the stress increase significantly is larger than that of GFCF (0.6 to 0.8), the difference can be explained in terms of the overall

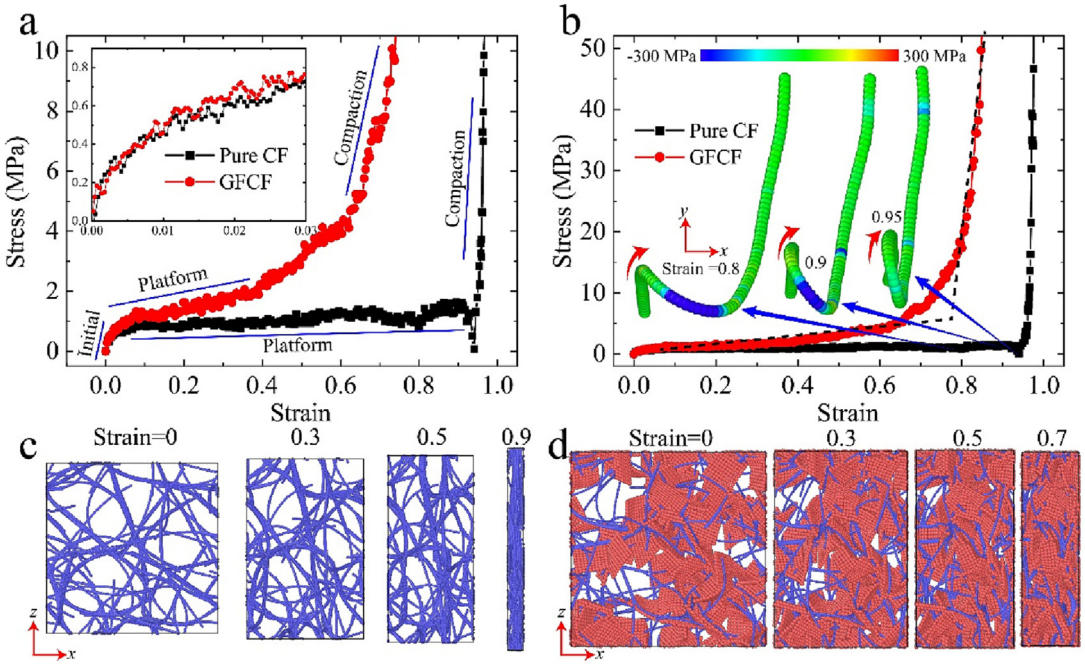

Fig. 2. Constitutive relation and typical snapshots of pure CF and GFCF under compression. (a) The compressive stress–strain curves of pure CF and GFCF, the inset is the amplification of the curves in the initial stage. (b) The compressive stress–strain curves of pure CF and GFCF with larger stress, the insets are the typical snapshots of CNT, color-coded by the normal stress in the *x* direction. (c) Typical snapshots of pure CF under the compressive strains of 0, 0.3, 0.5, and 0.9. (d) Typical snapshots of GFCF under the compressive strains of 0, 0.3, 0.5, and 0.7.

configurational evolution shown in Fig. 2c and d. The structure of pure CF is similar to dispersive spaghetti, and the structure of GFCF is similar to spaghetti filled with dressing, both structures become tighter as the foams are compressed. Typical structures show that the GFCF is almost compacted at a strain near 0.7, but the entire structure of pure CF is not compacted until the strain exceeds 0.9.

3.2. The deformation energy of pure CF and GFCF

The deformation energy of pure CF and GFCF under compression is further calculated to find the main deformation form. Under compression, the external work is converted into energy stored in the material, and the energy stored inside the material through deformation is called deformation energy. The deformation energy of graphene includes the stretching, bending, and shearing energy, while the deformation energy of CNTs only includes the stretching and bending energy due to the neglection of shearing energy in the coarse-grained model of CNT [41].

The deformation energy of pure CF and GFCF as a function of strain are shown in Fig. 3a, and the snapshots colored-coded by the deformation energy under a typical strain of 0.5 are illustrated in Fig. S4 of Supplemental Materials. As shown in Fig. 3a-I, the stretching energy of CNT in pure CF increases from 3216.6 eV to 9684.5 eV as the strain increase to about 0.95, the final stretching energy is about 3.01 times the initial stretching energy, while the shearing energy changes are almost negligible. This is consistent with the snapshots shown in Fig. S4a, even under a larger strain of 0.5, the CNT stretching energy is almost negligible compared to the CNT bending energy in pure CF, indicating that the compression properties of pure CF are mainly determined by the bending resistance of CNTs.

The deformation energy of graphene and CNT in GFCF is shown in Fig. 3a-II, where the bending energy of CNT is 1.98 to 2.87 times as much as the bending energy of graphene, and the bending energy of CNT is about 2.27 to 5.33 times as much as the shearing energy of graphene; not to mention the negligible stretching energy of CNT and graphene. Even at larger strains over 0.5, the stretching energy of graphene slightly increases, but is still significantly less than all the shearing and bending energy; the shearing energy of graphene increases to a value close to the bending energy of graphene, but is still much smaller than CNT bending energy. The conclusions are consistent with the visualized snapshots shown in Fig. S4 b and c of Supplemental Materials, indicating that the bending energy, especially the bending energy of CNT, dominates the compression of GFCF. Therefore, the CNT bending energy in pure CF and GFCF is extracted from Fig. 3a-I and II respectively and is uniformly plotted in Fig. 3a-III for comparison. Interestingly, the bending energy of CNT in GFCF is always larger than that in pure CF.

The comparison of deformation energy in Fig. 3a indicates that the larger intermediate modulus of GFCF compared with pure CF may be contributed by three aspects: (i) the significant increased CNT bending energy in GFCF compared with that in pure CF as shown in Fig. 3a-III, which should be dominated; (ii) the considerable graphene bending energy that is not present in pure CF, which may be the second reason; (iii) the small shearing and stretching energy of graphene, which only contributes at larger strain surpass 0.7.

The latter two contributions are easy to understand, compared with a pure CF containing CNTs only, the extra graphene in GFCF can also bear some compressing force. As depicted by the snapshots of the typical graphene flake shown in Fig. 3b-I to III, the graphene flake rolls into a mass like a piece of gauze scarf as strain increases. The snapshots of the graphene color-coded by its stretching, shearing, and bending energy at the strains of 0.5 and 0.8 are shown in Fig. 3c and d, respectively. The snapshots color-coded by different color bar ranges are also shown in Fig. S5. It shows that the red and green beads in Fig. 3c-III are more than that in Fig. 3c-I and II, while the number of red and green beads in Fig. 3-d-II and -III is about the same, but more than that in Fig. 3d-I, which is also consistent with the conclusion verified in Fig. 3a-II that the bending energy is dominant in graphene deformation

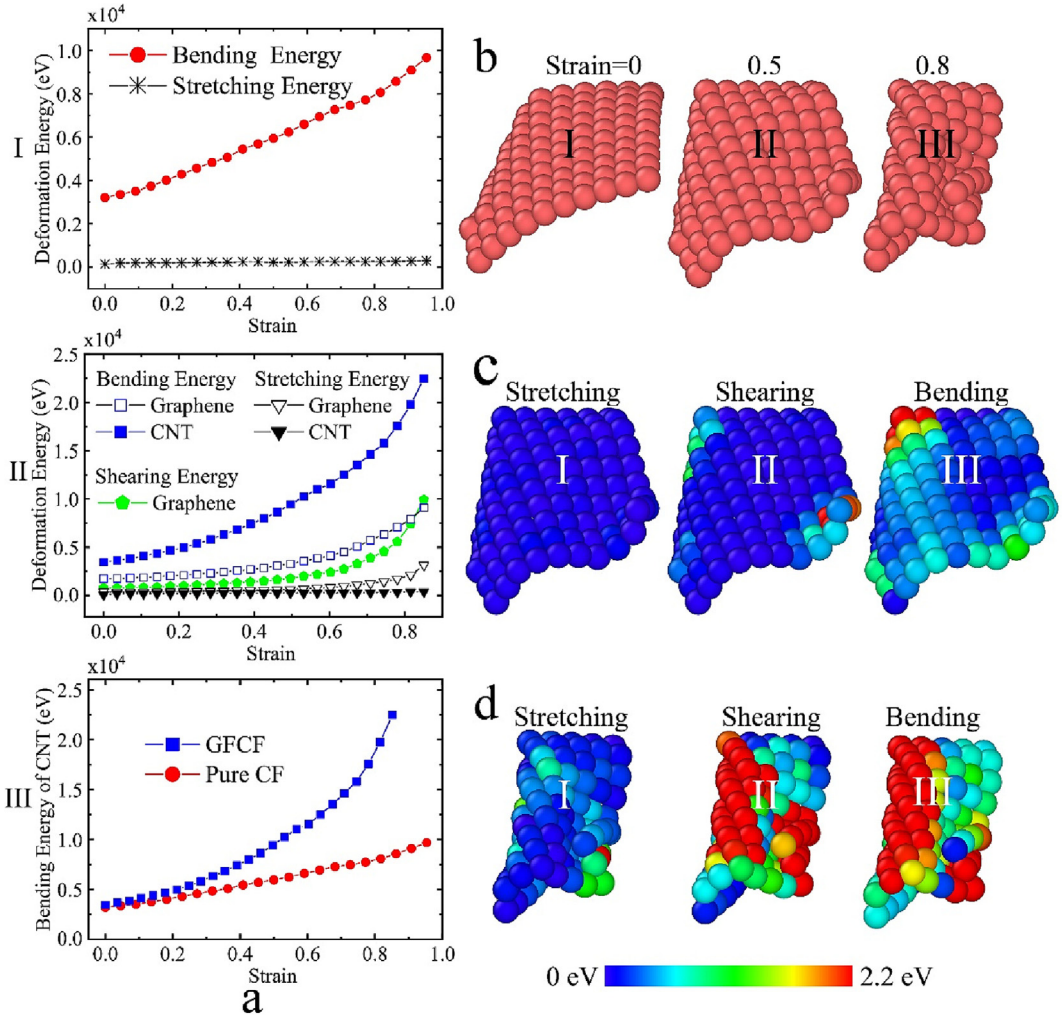

Fig. 3. The deformation energy of pure CF and GFCF. (a) The deformation energy of pure CF and GFCF as a function of strain; I: the deformation energy of CNT in pure CF; II: the deformation energy of graphene and CNT in GFCF; III: the bending energy of CNT in GFCF and pure CF. (b) The microscopic deformation of a graphene flake at strains of (I) 0, (II) 0.5, and (III) 0.8. (c) The snapshots of the graphene flake at the strain of 0.5 that color-coded by (I) stretching, (II) shearing, and (III) bending energy. (d) The snapshots of the graphene flake at the strain of 0.8 that color-coded by (I) stretching, (II) shearing, and (III) bending energy. The graphene beads in (c) and (d) are colored according to their bending energy.

energy at a small strain of 0.5, while both the bending and shearing energies appreciably contribute to the graphene deformation energy at a large strain of 0.8.

3.3. The structural dispersity of pure CF and GFCF

The snapshot of GFCF color-coded by bending energy at the strain of 0.5 is illustrated in Fig. 4a-I, where red and green are mostly found on CNT beads, while graphene beads are predominantly blue, further confirming that the CNTs bear the main bending energy. To show the bending energy distribution on CNT more clearly and completely, the snapshot of the CNT in GFCF color-coded by bending energy is shown separately in Fig. 4a-II, and a pure CF color-coded by bending energy is illustrated in Fig. 4a-III as a contrast, both of which include 100 CNT chains, while the CNTs in GFCF is thicker than that in pure CF. The red and green CNT beads in GFCF shown in Fig. 4a-II seem to be more than that in pure CF shown in Fig. 4a-III, indicating that the CNT in GFCF has higher bending energy, consistent with the quantitative statistics in Fig. 3a-III.

In addition, it can also be concluded from Fig. 4a-II and -III that the CNTs in GFCF mainly exist in the form of dispersed CNTs, while CNT bundles consisting of several CNTs are widespread in pure CNT. The strong aggregation of CNT in pure CF and the hindering effect of graphene on the aggregation behavior of CNT in graphene/CNT composite foams have also been observed in the previous literature [16], while the corresponding mechanism of how graphene increases the dispersion of CNT has not been revealed in detail.

By observing the relaxation process of the foams, two mechanisms by which graphene increases the dispersity of CNT are discovered, i.e., the adhesion and separation mechanisms. The adhesion mechanism is shown in Fig. 4b and c. Initially, two CNTs in pure CF intersect with each other, then they converge into a bundle after relaxation, as shown in Fig. 4b. While in GFCF as shown in Fig. 4c, the CNT labeled C_2 adheres to the graphene surface initially, after the relaxation, the CNT labeled C_1 also gradually adheres to the graphene surface due the attraction from graphene. The two CNTs will not be able to converge together due to the adhesive attraction from graphene, even if they are close to each other. To explore why graphene can hinder the aggregation of

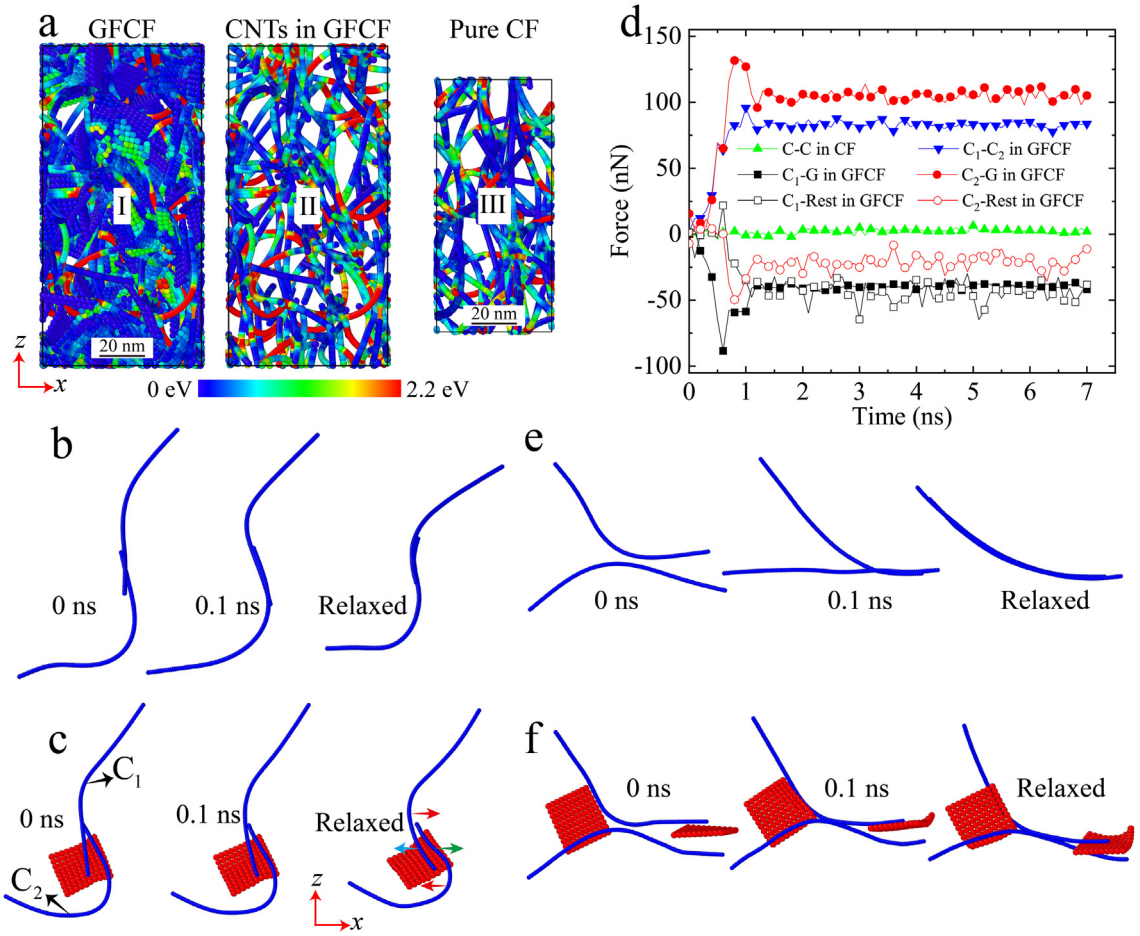

Fig. 4. The role of graphene in the dispersity of CNT and its mechanism. (a) The snapshots of pure CF and GFCF under the strain of 0.5, I: the graphene and CNT in GFCF; II: the CNTs in GFCF, graphene is not shown; III: the CNT in pure CF. The graphene and CNTs are colored according to their bending energy. (b-c) The adhesion mechanism of CNT dispersion, (b) typical CNT bundle in pure CF; (c) dispersed CNTs in GFCF due to the adhesive attraction from graphene. (d) The interaction force between graphene-CNT and CNT-CNT in pure CF and GFCF, the force in the *x* direction is defined as positive, C_1-G represents the interaction force exerted by graphene on the CNT labeled C_1. (e-f) The separation mechanism of CNT dispersion by graphene, (e) another typical CNT bundle in pure CF; (f) dispersed CNTs in GFCF due to the separation effect from graphene.

CNTs, the interaction forces between the graphene and the two CNTs are calculated, as shown in Fig. 4d, the force in the *x* direction is defined as positive. After the relaxation, the force exerted by C_2 on C_1 (labeled as C_1-C_2) is directed towards C_2, which means the two CNTs are attracted to each other. The graphene exerts a force on C_1 towards -*x* directions (labeled as C_1-G). Besides, C_1 is also affected by other neighboring graphene and CNTs as shown in Fig. S6 of Supplemental Materials, and the resultant force from the rest of the graphene and CNT are labeled as C_1-Rest. The C_1 is approximately balanced under the affection of C_1-C_2, C_1-G, and C_1-Rest. Similarly, C_2 is also balanced under the forces of C_2-C_1, C_2-G, and C_2-Rest. Therefore, the two CNTs will not converge together.

The separation mechanism is shown in Fig. 4e and f. Fig. 4e shows another example of CNT aggregating into a bundle in pure CF, while in GFCF, graphene flakes sandwiched between the CNTs prevent them from aggregating as shown in Fig. 4f. In summary, whether the CNTs are adhered to the same surface of graphene or separated on two sides of graphene, graphene can effectively prevent CNTs from agglomerating, and thus increases their dispersity.

3.4. The microscopic deformation mechanisms of pure CF and GFCF

To find out the relationship between the dispersity of CNT and their bearing capacity in GFCF, the snapshots of typical CNT net-

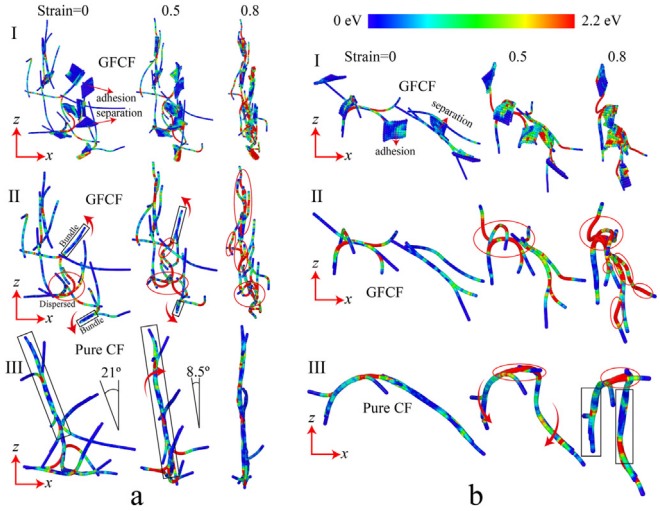

Fig. 5. Microscopic deformation of typical structure in pure CF and GFCF. (a) The deformation of a vertical structure under different strains of 0, 0.5, and 0.8; (I) the graphene and CNTs in GFCF; the CNT network in (II) GFCF and (III) pure CF. (b) The deformation of a horizontal structure under different strains of 0, 0.5, and 0.8; (I) the graphene and CNT in GFCF; the CNT network in (II) GFCF and (III) pure CF. All graphene flakes GFCF are not shown. All CNT networks are colored according to their bending energy with the unit of eV.

works color-coded by their bending energy in GFCF and pure CF under compression are investigated. A nearly vertical structure of GFCF is shown in Fig. 5a-I, which are color-coded by their bending energy. To clearly show the structure of the CNT network and the bending energy distribution on it, the CNT network in GFCF is separately shown in Fig. 5a-II, as a contrast, the CNT network in pure CF is shown in Fig. 5a-III. Many CNTs in GFCF adhere to and are separated by graphene as shown in Fig. 5a-I, making the CNT network in GFCF (Fig. 5a-II) more dispersive compared with that in pure CF (Fig. 5a-III). The CNT bundles in GFCF are rare and usually consist of only two or three CNTs as indicated in the black rectangles, which rotate to a more vertical direction as indicated by the arrows.

Meanwhile, more green and red appear on the dispersed CNTs at larger strain, as labeled in the red ellipse in Fig. 5a-II, indicating an increasing bending deformation on the dispersed CNTs with increasing strain. However, CNTs in pure CF tend to aggregate into CNT bundles as verified in Fig. 4, which leads to obvious rotation behavior in pure CF. As shown in Fig. 5a-III, the main bundle labeled in the black rectangle is composed of more than five CNTs, which is initially about 21° from the *z*-axis. As the pure CF compresses in the *x*-direction, more CNTs adhere to the main bundle. The main bundle gradually rotates to an angle of 8.5° with the *z*-axis at a strain of 0.5 and becomes almost along the *z*-axis at a strain of 0.8.

A similar phenomenon has also been observed on a horizontal CNT network. As shown in Fig. 5a-I, the CNTs in GFCF are adhered to and separated by graphene, hence the horizontal CNT network in GFCF (as shown in Fig. 5b-II) is also more dispersive than that in pure CF (as shown in Fig. 5b-III). As the GFCF compresses, green and red gradually appear on the dispersed CNTs as labeled in the ellipses of Fig. 5b-II, indicating that the bending deformation on CNT is gradually increasing, which is the main factor in transmitting and supporting the compressive loading. On the contrary, the CNT network tends to agglomerate into one CNT bundle as shown in Fig. 5b-III. As the pure CF compresses, both ends of the CNT bundle gradually rotate along the direction indicated by the arrows, and finally rotate into a nearly vertical direction as labeled in the two rectangles with almost negligible bending energy. The only remaining bending energy appears in the middle of the CNT bundle as labeled in the ellipse.

To understand the role of graphene in GFCF, the rearrangement of the CNT bundle in pure CF and the deformation of graphene-fixed CNTs are illustrated in Fig. 6. As shown in Fig. 6a-I, the CNTs labeled "1″ and "2" are approximately parallel, and the linear contact caused by Van der Waals forces between them forces them to aggregate into a CNT bundle. The CNT bundle intersects with CNT "3", the point contact formed by their intersection limits the displacement of the CNT bundle, which can be simplified as hinge support. As the strain increases to 0.5, the CNT bundle will be extruded by other CNTs. However, due to the hinge support formed by CNT "3", it will rotate as shown in Fig. 6a-II. The rotation could be simplified as the schematic diagram shown in Fig. 6b, where the beam constrained by hinge support can rotate freely under the action of an external force.

However, the CNTs in GFCF become more dispersed and can withstand more bending energy as discussed in Figs. 3–5. As shown in Fig. 6c-I, although the line contact (marked in the rectangle) makes the CNT "1″ and "2" tend to form a CNT bundle, they remain dispersed due to the adhesion of graphene "3" and "4". On the one hand, the dispersed structure allows the CNTs to be distributed in more different directions, especially along the *x*-direction marked in the ellipse. On the other hand, graphene may act as fixed support to limit the movement and rotation of CNT, such as the graphene "3", "4", and "5". When the GFCF is compressed along the *x*-direction, the graphene-fixed CNT composed of CNT "1" and graphene "3" can be simplified as a cantilever beam as shown in Fig. 6d, which is subjected to a load parallel to its axis, resulting in buckling deformation; the graphene-fixed CNT composed of CNT "2", graphene "4" and "5" can be regarded as a statically indeterminate beam fixed at both ends as shown in Fig. 6e, which is subjected to a force perpendicular to its axis, leading to

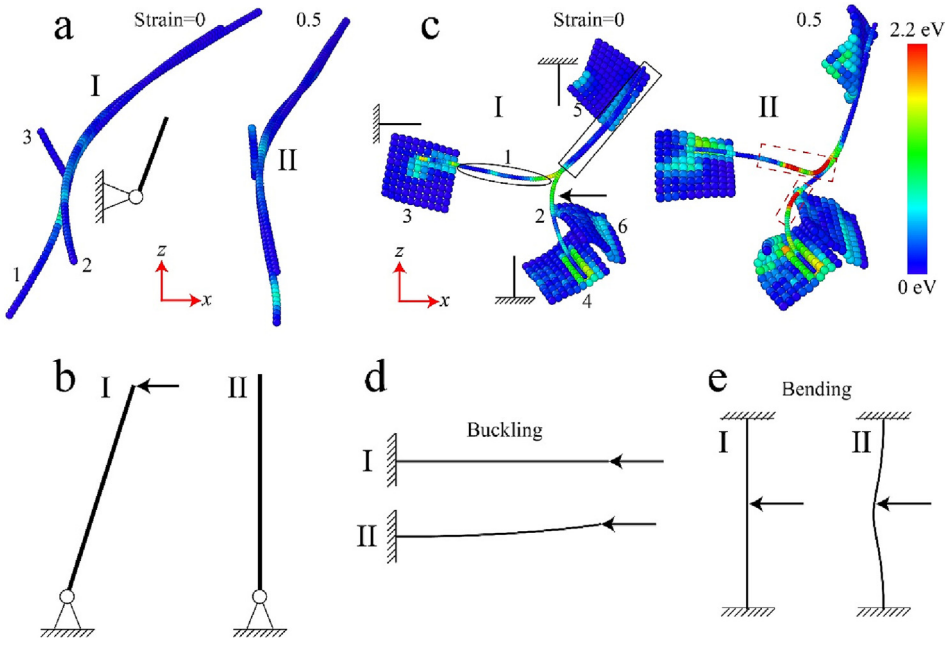

Fig. 6. The role of graphene on the rearrangement and deformation of CNT. (a) The rearrangement of CNT in pure CF; the snapshots of the CNT bundle at strains of (I) 0 and (II) 0.5, respectively. (b) The (I) initial and (II) final schematic diagram of the rearrangement of the CNT bundle in pure CF. (c) The deformation of CNT in GFCF; the snapshots of graphene-fixed CNTs in GFCF at strains of (I) 0 and (II) 0.5, respectively. (d-e) The initial and final schematic diagram of the buckling and bending of graphene-fixed CNTs in GFCF. The graphene and CNTs in (a) and (c) are colored according to their bending energy with the unit of eV.

bending deformation of the CNT. Both buckling and bending deformation lead to increasing CNT bending energy as shown in Fig. 6c-II.

In pure CF, the line contact between CNTs makes them form CNT bundles, and the point contacts form many hinge supports. As the pure CF is compressed, the CNT bundles rearrange themselves in the form of rotating, hence the external work is rarely stored in the materials as deformation energy, leading to a smaller intermediate modulus. In GFCF, CNTs mainly exist in the form of dispersed CNTs, whose bending stiffness is smaller than CNT bundles and is easier to store external work through deformation. In addition, the graphene act as fixed support limiting both movement and rotation of CNTs, making CNTs more inclined to store bending energy through bending and buckling deformation, thus increasing the compressive properties of the whole materials.

3.5. The effects of graphene number on the structural dispersity and mechanical property

The influence of the number of graphene flakes on the dispersity and compressive modulus of foams is further investigated. As shown in Fig. 7a, the stress of the GFCF is always higher than the foam without graphene (i.e., pure CF). When the number of graphene flakes is less than 100, the stress of GFCF increases with the number of graphene flakes; but when the number of graphene flakes exceeds 100, the stress does not increase anymore. The initial and intermediate modulus of foams in the initial and platform stage is calculated based on the stress–strain curves, respectively. As shown in Fig. 7b, the initial modulus did not change significantly with the increase of the number of graphene flakes, but the intermediate modulus increases more than sixfold as the number of graphene flakes increases to 100, then does not change significantly with increasing graphene number. Therefore, 100 is the optimal filling number of graphene in the GFCF containing 100 CNT chains.

Under a smaller strain of less than 0.02, i.e., in the initial stage, no microstructural evolution and rearrangement occur [43], and the stiffness of foam is mainly derived from the intrinsic properties of its components [18–20], including the main component CNTs that act as a skeleton and the minor component graphene that act as fillers. An increase in the number of graphene flakes, as a minor component, would of course have little effect on the initial modulus.

To reveal the influencing mechanism of the number of graphene flakes on the intermediate modulus, the relationship between the CNT dispersity and the number of graphene flakes should be confirmed first. The amount of the CNT bundles and the contact area between the CNTs are positively correlated, therefore, the contact area between CNTs, as well as the contact area between graphene flakes, and between CNTs and graphene flakes are calculated and denoted as C-C, G-G, and C-G, respectively. As shown in Fig. 7c, when the number of graphene flakes is less than 100, the contact area between graphene flakes, and between CNTs and graphene flakes both increase with increasing numbers of graphene flakes. What's more, the contact area between CNTs decreases with an increasing number of graphene flakes, indicating that the CNTs in GFCF become more dispersed with increasing graphene number. Furthermore, both contact area between CNTs and between graphene and CNTs approaches a constant when the number of graphene flakes exceeds 100, while the contact area between graphene still continuously increases.

The underlying mechanism is easy to understand, as shown in Fig. 7d-I, The CNTs in pure CF exist in the form of bundles, but when 50 graphene flakes are introduced, as shown in Fig. 7d-II, the top two CNTs marked 1 and 2 are separated from the bundle due to the adhesion of the two yellow graphene. As the number of graphene flakes increases to 100, the bottom two CNT marked 3 and 4 are separated by the additional red graphene as shown in Fig. 7d-III. Thus, CNTs become more dispersed as the number of graphene flakes increases. In the meantime, the CNTs are con-

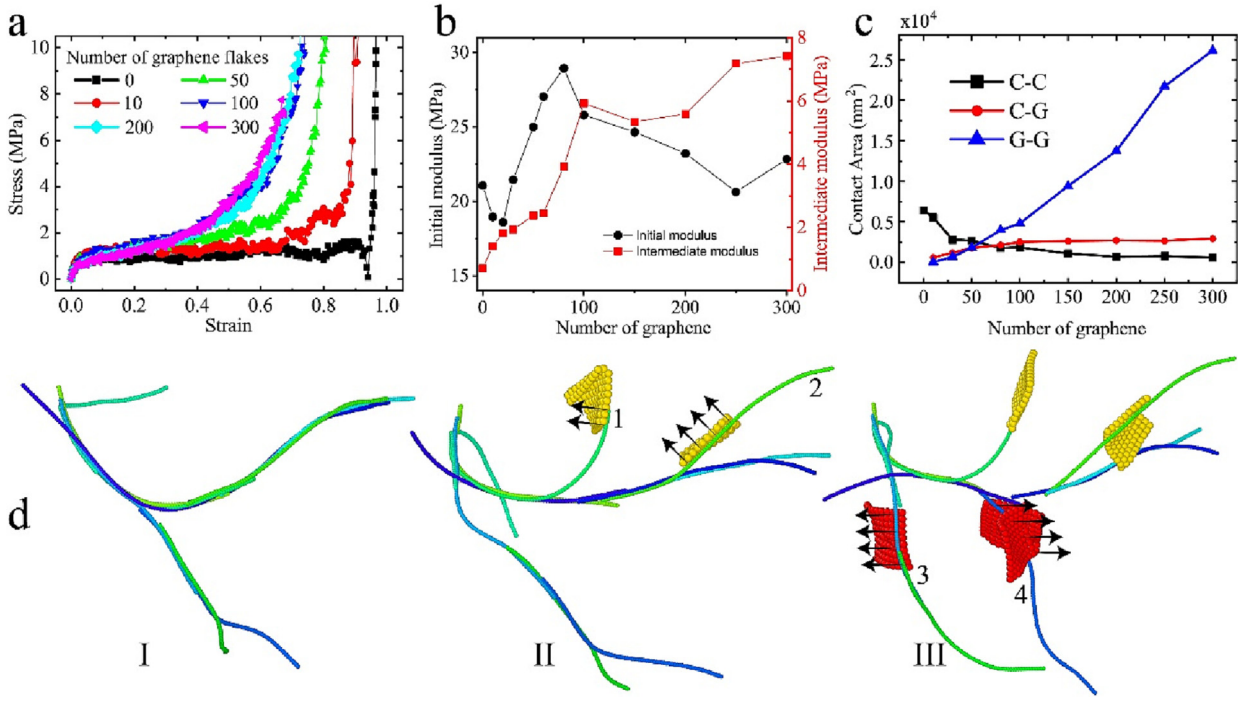

Fig. 7. The effect of the number of graphene flakes. (a) The stress–strain relationship of pure CF and GFCF containing varying numbers of graphene flakes. (b) The initial and intermediate modulus of foams as a function of the number of graphene flakes. (c) The contact area in the foams as a function of the number of graphene flakes, the contact area between CNTs, between graphene flakes, and between CNTs and graphene flakes are denoted as C-C, G-G, and C-G, respectively. (d) The initial microstructure of the CNT network in (I) pure CF and GFCF containing (II) 50 and (III) 100 graphene flakes.

strained by more fixed ends of graphene with increasing graphene number, resulting in increasing buckling and bending deformation of CNT and intermediate modulus of GFCF. However, as the number of graphene flakes increases further, the additional graphene will aggregate with graphene, but will not make CNT more dispersed, and will not form more fixed ends to limit the movement and rotation of CNTs, so the stress does not increase further.

3.6. The effects of graphene thickness on the structural dispersity and mechanical property

Unlike the significant effect of the number of graphene flakes on the dispersity and mechanical properties, we found that the thickness of graphene has a very limited effect on dispersity and mechanical properties. As shown in Fig. 8a, the GFCFs are all composed of 100 CNTs and 30 graphene flakes, the difference comes from the thickness of graphene, which contains 1-, 2-, 4-, and 8-layer graphene. The corresponding parameters of the coarse-grained model of 2-, 4-, and 8-layer graphene can be acquired in our previous works [20,43]. The four curves are close to almost coincidental in the platform stage, while the initial modulus in the initial stage slightly increases with the graphene thickness. Even for GFCF with more graphene flakes, such as the stress–strain curves of GFCF containing 100 CNTs and 100 graphene flakes shown in Fig. 8b, the stress of GFCF only slightly increases with the thickness of graphene.

The phenomenon is consistent with previous results conducted in Figs. 3-5 that the initial modulus is determined by the intrinsic properties of both CNT and graphene, while the intermediate modulus is mainly determined by the bending energy of CNTs and partly affected by other deformation energy. In the initial stage, the intrinsic resistance to the deformation of graphene increases as the thickness of graphene increases, hence the corresponding initial modulus increases. In the platform stage, the bending energy of graphene also contributes a little, thus the stress tends to slightly increase with graphene thickness. In summary, graphene affects the foams mainly by increasing the dispersity of CNT and impeding the rearrangement of dispersed CNTs, while its intrinsic properties have limited influence on the whole material, hence the effect on the foam is more pronounced by the number of graphene flakes rather than the thickness.

In this paper, the GFCF is composed of longer 1D CNTs and smaller 2D graphene, in which graphene improves the compressive properties of the foam by hindering the agglomeration of CNTs and limiting the rotation and deformation of CNTs. We further demonstrate that this phenomenon and conclusion still hold when graphene is replaced by hold-graphene or rectangular graphene, see Fig. S7 of Supplemental Materials for a detailed discussion. Therefore, we believe the microscopic deformation mechanism obtained in this paper can be extended to other foam materials consisting of longer 1D nanowires and smaller 2D flakes.

4. Conclusions

In this paper, we constructed coarse-grained numerical models of GFCF to investigate the role of graphene in GFCF under compression and the corresponding deformation mechanism. It shows that graphene enhances the compressive properties of the GFCF mainly by changing the dispersity and deformation of CNTs so that the buckling and bending rigidity of CNTs can be fully exploited, but partly by the graphene's ability to transfer loading through deformation. The CNTs in pure CF tend to form bundles due to the large Van der Waals force between CNT in line contact, and the point contacts between them act as the hinge supports constraining the movement of CNT bundles. Under compression, the CNT bundles rearrange freely in the form of rotation around the hinge supports, resulting in lower compressive stress. When graphene is introduced into composite foams, CNTs tend to exist in the form of dispersed CNTs due to the adhesion or separation effect of graphene, hence more CNTs are loaded by buckling deformation along the compression direction; and graphene also limits the rotation of CNTs, allowing it to carry the load through bending deformation, both buckling and bending deformation stores bending energy in CNT, leading to a larger intermediate modulus of the whole materials. As the number of graphene flakes increases, the CNTs become more dispersed due to the adhesion and separation of more graphene and are constrained by more fixed ends of graphene, leading to increasing buckling and bending deformation of CNT and intermediate modulus of GFCF. However, as the thickness of graphene increases, the microstructure form of CNTs hardly changes, graphene can only affect the compressive modulus by transferring loads through its deformation, resulting in a very limited improvement in the compressive performance. The results in this paper provide a numerical paradigm for the compressive properties of 3D foam materials composed of 1D and 2D materials, and the microscopic deformation mechanism obtained in this paper can be extended to other foam materials consisting of longer 1D nanowires and smaller 2D flakes.

5. Methods

5.1. The contact area

Two graphene beads are defined as touching graphene beads if they are close to each other and belong to different graphene

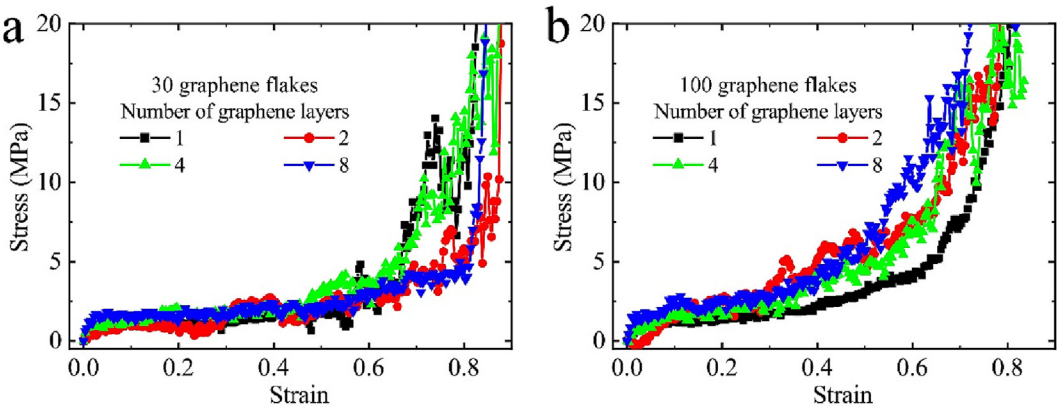

Fig. 8. The effect of the thickness of graphene. (a) The stress–strain curves of GFCF containing 100 CNT chains and 30 graphene flakes; (b) The stress–strain curves of GFCF containing 100 CNT chains and 100 graphene flakes. Four different thicknesses of graphene flakes, i.e., 1-, 2-, 4-, and 8-layer graphene, are considered.

flakes, the area of the graphene flakes occupied by the touching graphene bead is the contact area of the touching graphene bead. The contact area between graphene flakes is the sum of the contact area of the touching graphene beads. Similarly, The contact area between CNTs as well as the contact area between CNTs and graphene flakes are the sum of the contact area of corresponding touching beads. To simplify the calculation, the contact area of a touching CNT bead is defined as the axial cross-section of a single-walled CNT, rather than the lateral area of the actual contact.

5.2. The normal stress

The virial stress is viewed as a measure of the stress on the micro/mesoscale, the virial stress on the atom i can be calculated according to $\sigma_{XX} = \frac{1}{V}\sum_i \left[\frac{1}{2}\sum_{j=1}^{N}\left(R_X^j - R_X^i\right)F_X^{ij} + m^i v_X^i v_X^i\right]$, in which V is the volume of one atom, R_X^α and R_X^β denote the positions of atoms α and β in X-axis. $F_X^{\alpha\beta}$ is the force acted on atom i induced by atom j in the X direction, m^i is the mass of atoms i, v_X^i is the velocity of atom i in the X-axis, V is the volume of atoms i.

Author contributions

S.W. conceived the original idea, carried out all simulations, and drafted the paper. S.H. C. and L.H. L. supervised the study and revised the paper. All of the authors contributed to the discussions and reviewed the manuscript.

Data availability

Data will be made available on request.

Declaration of Competing Interest

The authors declare that they have no known competing financial interests or personal relationships that could have appeared to influence the work reported in this paper.

Acknowledgements

This work is supported by the National Natural Science Foundation of China through Grants #12002034, #12172035, #92160203, #11872114, and #12032004, and the Fundamental Research Funds for the Central Universities of China (buctrc201930).

Appendix A. Supplementary data

Supplementary data to this article can be found online at https://doi.org/10.1016/j.matdes.2023.112043.

References

[1] S. Iijima, Helical microtubules of graphitic carbon, Nature 354 (6348) (1991) 56–58.
[2] K.S. Novoselov, A.K. Geim, S.V. Morozov, D. Jiang, Y. Zhang, S.V. Dubonos, I.V. Grigorieva, A.A. Firsov, Electric field effect in atomically thin carbon films, Science 306 (5696) (2004) 666–669.
[3] W. Yang, H. Bai, B. Jiang, C. Wang, W. Ye, Z. Li, C. Xu, X. Wang, Y. Li, Flexible and densified graphene/waterborne polyurethane composite film with thermal conducting property for high performance electromagnetic interference shielding, Nano Res.. 15 (11) (2022) 9926–9935.
[4] L. Li, J. Xu, G. Li, X. Jia, Y. Li, F. Yang, L. Zhang, C. Xu, J. Gao, Y. Liu, Z. Fang, Preparation of graphene nanosheets by shear-assisted supercritical CO2 exfoliation, Chem. Eng. J. 284 (2016) 78–84.
[5] L. Qiu, B. Huang, Z. He, Y. Wang, Z. Tian, J.Z. Liu, K. Wang, J. Song, T.R. Gengenbach, D. Li, Extremely Low Density and Super-Compressible Graphene Cellular Materials, Adv. Mater. 29 (36) (2017) 1701553.
[6] X. Gui, J. Wei, K. Wang, A. Cao, H. Zhu, Y. Jia, Q. Shu, D. Wu, Carbon Nanotube Sponges, Adv. Mater. 22 (5) (2010) 617–621.
[7] N. Anzar, R. Hasan, M. Tyagi, N. Yadav, J. Narang, Carbon nanotube - A review on Synthesis, Properties and plethora of applications in the field of biomedical science, Sensors, International 1 (2020) 100003.
[8] S. Han, D. Wu, S. Li, F. Zhang, X. Feng, Porous graphene materials for advanced electrochemical energy storage and conversion devices, Adv. Mater. 26 (6) (2014) 849–864.
[9] M.A. Worsley, S.O. Kucheyev, J.H. Satcher, A.V. Hamza, T.F. Baumann, Mechanically robust and electrically conductive carbon nanotube foams, Appl. Phys. Lett. 94 (7) (2009) 073115.
[10] D. Hu, W. Gong, J. Di, D. Li, R. Li, W. Lu, B. Gu, B. Sun, Q. Li, Strong graphene-interlayered carbon nanotube films with high thermal conductivity, Carbon 118 (2017) 659–665.
[11] Y. Wu, J. Zhu, L. Huang, A review of three-dimensional graphene-based materials: Synthesis and applications to energy conversion/storage and environment, Carbon 143 (2019) 610–640.
[12] R. You, Y.-Q. Liu, Y.-L. Hao, D.-D. Han, Y.-L. Zhang, Z. You, Laser Fabrication of Graphene-Based Flexible Electronics, Adv. Mater. 32 (15) (2020) 1901981.
[13] Z. Yang, J. Tian, Z. Yin, C. Cui, W. Qian, F. Wei, Carbon nanotube- and graphene-based nanomaterials and applications in high-voltage supercapacitor: A review, Carbon 141 (2019) 467–480.
[14] X. Wu, Z. Li, Y. Zhu, J. Wang, S. Yang, Ultralight GO-Hybridized CNTs Aerogels with Enhanced Electronic and Mechanical Properties for Piezoresistive Sensors, ACS Appl. Mater. Interfaces 13 (22) (2021) 26352–26361.
[15] S.P. Patil, V.G. Parale, H.-H. Park, B. Markert, Mechanical modeling and simulation of aerogels: A review, Ceram. Int. 47 (3) (2021) 2981–2998.
[16] H. Sun, Z. Xu, C. Gao, Multifunctional, ultra-flyweight, synergistically assembled carbon aerogels, Adv. Mater. 25 (18) (2013) 2554–2560.
[17] F. Guo, Y. Jiang, Z. Xu, Y. Xiao, B. Fang, Y. Liu, W. Gao, P. Zhao, H. Wang, C. Gao, Highly stretchable carbon aerogels, Nat. Commun. 9 (1) (2018) 881.
[18] J. Sha, R.V. Salvatierra, P. Dong, Y. Li, S.-K. Lee, T. Wang, C. Zhang, J. Zhang, Y. Ji, P.M. Ajayan, J. Lou, N. Zhao, J.M. Tour, Three-Dimensional Rebar Graphene, ACS Appl. Mater. Interfaces 9 (8) (2017) 7376–7384.
[19] S. Vinod, C.S. Tiwary, L.D. Machado, S. Ozden, R. Vajtai, D.S. Galvao, P.M. Ajayan, Synthesis of ultralow density 3D graphene–CNT foams using a two-step method, Nanoscale 8 (35) (2016) 15857–15863.
[20] S. Wang, C. Wang, M.B. Khan, S. Chen, Microscopic deformation mechanism and main influencing factors of carbon nanotube coated graphene foams under uniaxial compression, Nanotechnology 32 (34) (2021) 345704.
[21] Z. Yan, Z. Peng, G. Casillas, J. Lin, C. Xiang, H. Zhou, Y. Yang, G. Ruan, A.-R.-O. Raji, E.L.G. Samuel, R.H. Hauge, M.J. Yacaman, J.M. Tour, Rebar Graphene, ACS Nano 8 (5) (2014) 5061–5068.
[22] E.F. Hacopian, Y. Yang, B. Ni, Y. Li, X. Li, Q. Chen, H. Guo, J.M. Tour, H. Gao, J. Lou, Toughening Graphene by Integrating Carbon Nanotubes, ACS Nano 12 (8) (2018) 7901–7910.
[23] W. Zhang, H. Xie, R. Zhang, M. Jian, C. Wang, Q. Zheng, F. Wei, Y. Zhang, Synthesis of three-dimensional carbon nanotube/graphene hybrid materials by a two-step chemical vapor deposition process, Carbon 86 (2015) 358–362.
[24] Y. Zhu, L. Li, C. Zhang, G. Casillas, Z. Sun, Z. Yan, G. Ruan, Z. Peng, A.-R.-O. Raji, C. Kittrell, R.H. Hauge, J.M. Tour, A seamless three-dimensional carbon nanotube graphene hybrid material, Nat. Commun. 3 (92) (2012) 1–7.
[25] Y. Wang, Y. Zhu, F. Wang, X. Liu, H. Wu, Super-elasticity and deformation mechanism of three-dimensional pillared graphene network structures, Carbon 118 (2017) 588–596.
[26] F.D. Novaes, R. Rurali, P. Ordejón, Electronic Transport between Graphene Layers Covalently Connected by Carbon Nanotubes, ACS Nano 4 (12) (2010) 7596–7602.
[27] G.K. Dimitrakakis, E. Tylianakis, G.E. Froudakis, Pillared Graphene: A New 3-D Network Nanostructure for Enhanced Hydrogen Storage, Nano Lett. 8 (10) (2008) 3166–3170.
[28] J. Kuang, Z. Dai, L. Liu, Z. Yang, M. Jin, Z. Zhang, Synergistic effects from graphene and carbon nanotubes endow ordered hierarchical structure foams with a combination of compressibility, super-elasticity and stability and potential application as pressure sensors, Nanoscale 7 (20) (2015) 9252–9260.
[29] K.H. Kim, Y. Oh, M.F. Islam, Graphene coating makes carbon nanotube aerogels superelastic and resistant to fatigue, Nat. Nanotechnol. 7 (9) (2012) 562–566.
[30] S. Wang, T. Yang, C. Wang, L. Liang, The mechanical response and microscopic deformation mechanism of graphene foams tuned by long carbon nanotubes and short crosslinkers, PCCP 25 (1) (2023) 192–202.
[31] X. Wu, F. Mu, H. Zhao, Recent progress in the synthesis of graphene/CNT composites and the energy-related applications, J. Mater. Sci. Technol. 55 (2020) 16–34.
[32] M.R. Zakaria, M.F. Omar, M.S. Zainol Abidin, H. Md Akil, M.M.A.B. Abdullah, Recent progress in the three-dimensional structure of graphene-carbon nanotubes hybrid and their supercapacitor and high-performance battery applications, Compos. A Appl. Sci. Manuf. 154 (2022) 106756.
[33] S.-Y. Yang, W.-N. Lin, Y.-L. Huang, H.-W. Tien, J.-Y. Wang, C.-C.-M. Ma, S.-M. Li, Y.-S. Wang, Synergetic effects of graphene platelets and carbon nanotubes on the mechanical and thermal properties of epoxy composites, Carbon 49 (3) (2011) 793–803.
[34] S. Kabiri, D.N.H. Tran, T. Altalhi, D. Losic, Outstanding adsorption performance of graphene–carbon nanotube aerogels for continuous oil removal, Carbon 80 (2014) 523–533.
[35] N. Bagotia, V. Choudhary, D.K. Sharma, Synergistic effect of graphene/multiwalled carbon nanotube hybrid fillers on mechanical,

electrical and EMI shielding properties of polycarbonate/ethylene methyl acrylate nanocomposites, Compos. B Eng. 159 (2019) 378–388.
[36] M. Ye, C. Hu, L. Lv, L. Qu, Graphene-winged carbon nanotubes as high-performance lithium-ion batteries anode with super-long cycle life, J. Power Sources 305 (2016) 106–114.
[37] M. Etesami, M.T. Nguyen, T. Yonezawa, A. Tuantranont, A. Somwangthanaroj, S. Kheawhom, 3D carbon nanotubes-graphene hybrids for energy conversion and storage applications, Chem. Eng. J. 446 (2022) 137190.
[38] S. Cranford, M.J. Buehler, Twisted and coiled ultralong multilayer graphene ribbons, Model. Simul. Mater. Sci. Eng. 19 (2011) 054003.
[39] S. Cranford, M.J. Buehler, Twisted and coiled ultralong multilayer graphene ribbons, Model. Simul. Mater. Sci. Eng. 19 (5) (2011) 054003.
[40] M.J. Buehler, Mesoscale modeling of mechanics of carbon nanotubes: self-assembly, self-folding, and fracture, J. Mater. Res. 21 (11) (2006) 2855–2869.
[41] S. Cranford, H. Yao, C. Ortiz, M.J. Buehler, A single degree of freedom 'lollipop' model for carbon nanotube bundle formation, J. Mech. Phys. Solids 58 (3) (2010) 409–427.
[42] C. Wang, D. Pan, S. Chen, Energy dissipative mechanism of graphene foam materials, Carbon 132 (2018) 641–650.
[43] C. Wang, C. Zhang, S. Chen, The microscopic deformation mechanism of 3D graphene foam materials under uniaxial compression, Carbon 109 (2016) 666–672.
[44] C. Wang, C. Zhang, S. Chen, Micro-mechanism and influencing factors of graphene foam elasticity, Carbon 148 (2019) 267–276.
[45] C. Wang, L. Wang, Z. Xu, Enhanced mechanical properties of carbon nanotube networks by mobile and discrete binders, Carbon 64 (2013) 237–244.
[46] C. Wang, B. Xie, Y. Liu, Z. Xu, Mechanotunable Microstructures of Carbon Nanotube Networks, ACS Macro Lett. 1 (10) (2012) 1176–1179.
[47] P. Liu, X. Li, X. Chang, P. Min, C. Shu, Y. Li, Y. Kang, Z.-Z. Yu, Highly anisotropic graphene aerogels fabricated by calcium ion-assisted unidirectional freezing for highly sensitive sensors and efficient cleanup of crude oil spills, Carbon 178 (2021) 301–309.
[48] D. Yu, L. Dai, Self-Assembled Graphene/Carbon Nanotube Hybrid Films for Supercapacitors, The Journal of Physical Chemistry Letters 1 (2) (2010) 467–470.
[49] H. Hu, Z. Zhao, W. Wan, Y. Gogotsi, J. Qiu, Ultralight and highly compressible graphene aerogels, Adv. Mater. 25 (15) (2013) 2219–2223.
[50] S. Park, K.-S. Lee, G. Bozoklu, W. Cai, S.T. Nguyen, R.S. Ruoff, Graphene Oxide Papers Modified by Divalent Ions—Enhancing Mechanical Properties via Chemical Cross-Linking, ACS Nano 2 (3) (2008) 572–578.
[51] Z. Chen, W. Ren, L. Gao, B. Liu, S. Pei, H.-M. Cheng, Three-dimensional flexible and conductive interconnected graphene networks grown by chemical vapour deposition, Nat. Mater. 10 (6) (2011) 424–428.
[52] S. Woo, Y.-R. Kim, T.D. Chung, Y. Piao, H. Kim, Synthesis of a graphene–carbon nanotube composite and its electrochemical sensing of hydrogen peroxide, Electrochim. Acta 59 (2012) 509–514.
[53] Y. Wang, Y. Zhu, H. Wu, Formation and topological structure of three-dimensional disordered graphene networks, PCCP 23 (17) (2021) 10290–10302.
[54] B. Xie, Y. Liu, Y. Ding, Q. Zheng, Z. Xu, Mechanics of carbon nanotube networks: microstructural evolution and optimal design, Soft Matter 7 (21) (2011) 10039–10047.
[55] J.J. Shang, Q.-S. Yang, X. Liu, C. Wang, Compressive deformation mechanism of honeycomb-like graphene aerogels, Carbon 134 (2018) 398–410.
[56] Y. Wang, Y. Zhu, H. Wu, Porous Characteristics of Three-Dimensional Disordered Graphene Networks, Crystals 11 (2) (2021) 127.
[57] W. Xie, Y. Wei, Roughening for Strengthening and Toughening in Monolayer Carbon Based Composites, Nano Lett. 21 (11) (2021) 4823–4829.
[58] K. Xiao, Q. Yin, X. Wu, C. Huang, Mechanical behavior of single-layer graphdiyne via supersonic micro-projectile impact, Nano, Mater. Sci. 4 (4) (2022) 383–392.
[59] K. Xiao, X. Lei, Y. Chen, Q. An, D. Hu, C. Wang, X. Wu, C. Huang, Extraordinary impact resistance of carbon nanotube film with crosslinks under micro-ballistic impact, Carbon 175 (2021) 478–489.
[60] Z. Ma, A. Wei, J. Ma, L. Shao, H. Jiang, D. Dong, Z. Ji, Q. Wang, S. Kang, Lightweight, compressible and electrically conductive polyurethane sponges coated with synergistic multiwalled carbon nanotubes and graphene for piezoresistive sensors, Nanoscale 10 (15) (2018) 7116–7126.
[61] S. Plimpton, Fast Parallel Algorithms for Short-Range Molecular Dynamics, J. Comput. Phys. 117 (1) (1993) 1–19.
[62] A. Stukowski, Visualization and analysis of atomistic simulation data with OVITO–the Open Visualization Tool, Model. Simul. Mater. Sci. Eng. 18 (1) (2010) 015012.